

RESEARCH ARTICLE | JUNE 03 2015

Lifecycle of laser-produced air sparks

S. S. Harilal; B. E. Brumfield; M. C. Phillips



Physics of Plasmas 22, 063301 (2015)

<https://doi.org/10.1063/1.4922076>

 CHORUS



View
Online



Export
Citation

CrossMark

Articles You May Be Interested In

Digital engineering and reengineering in the management of the full lifecycle of high-tech products

AIP Conference Proceedings (November 2022)

Lifecycle management of high-tech products based on modern information technologies

AIP Conference Proceedings (August 2022)

State of the art review on implementation of product lifecycle management in manufacturing and service industries

AIP Conference Proceedings (February 2021)



Physics of Plasmas

Features in Plasma Physics Webinars

Register Today!

 AIP
Publishing

Lifecycle of laser-produced air sparks

S. S. Harilal,^{a)} B. E. Brumfield, and M. C. Phillips

Pacific Northwest National Laboratory, P.O. Box 999, Richland, Washington 99352, USA

(Received 13 April 2015; accepted 22 May 2015; published online 3 June 2015)

We investigated the lifecycle of laser-generated air sparks or plasmas using multiple plasma diagnostic tools. The sparks were generated by focusing the fundamental radiation from an Nd:YAG laser in air, and studies included early and late time spark dynamics, decoupling of the shock wave from the plasma core, emission from the spark kernel, cold gas excitation by UV radiation, shock waves produced by the air spark, and the spark's final decay and turbulence formation. The shadowgraphic and self-emission images showed similar spark morphology at earlier and late times of its lifecycle; however, significant differences are seen in the midlife images. Spectroscopic studies in the visible region showed intense blackbody-type radiation at early times followed by clearly resolved ionic, atomic, and molecular emission. The detected spectrum at late times clearly contained emission from both CN and N₂⁺. Additional spectral features have been identified at late times due to emission from O and N atoms, indicating some degree of molecular dissociation and excitation. Detailed spatially and temporally resolved emission analysis provides insight about various physical mechanisms leading to molecular and atomic emission by air sparks, including spark plasma excitation, heating of cold air by UV radiation emitted by the spark, and shock-heating.

© 2015 AIP Publishing LLC. [http://dx.doi.org/10.1063/1.4922076]

I. INTRODUCTION

The study of laser breakdown sparks or plasmas has a long history, and research articles can be found on this topic since the first laser was invented in 1960s.^{1,2} Currently, laser ablation and laser plasmas are used for an enormous number of applications ranging from geological, biological, environmental, nuclear safeguards, and space exploration, to new emerging applications.^{2–4} Significant recent innovations in the use of laser ablation and laser plasmas in many applications are due to the advancements in laser technology (e.g., the availability of shorter pulse lasers), better diagnostic tools (e.g., higher space and time resolution, improved detectors) along with a better understanding of plasma physics and chemistry. An intense pulsed laser focused onto a sample of interest generates a plasma, which is a source of excited atoms, ions, molecules, nano-, and micro-particles. The plasma is rich in emitting electromagnetic radiation, and its emission spectrum can be controlled by manipulating the temperature of the plasma. However, the interaction of an intense laser with a solid or a gaseous medium is still far from a mature science; the extensive research in this field indicates the complexity of the laser-sample and laser-plasma interaction. For example, optical breakdown in air—which is one of the simplest systems— involves many phenomena including self-focusing, self-trapping, multi-photon and cascade ionization, inverse bremsstrahlung, radiation from the plasma, etc.⁵ In addition, many of these phenomena occur simultaneously, and direct independent measurement of each process is often impractical. Hence, the involved physical and chemical processes occurring during the air spark lifecycle are very complex and not yet fully understood.

The ambient conditions (composition, temperature, and pressure of the gas in which the breakdown occurs) affect the hydrodynamic expansion features of the laser plasma explosion greatly. In the presence of moderate to high ambient pressures (≥ 100 mTorr), a shock wave is formed at the interface between the plasma and ambient medium and will continue to expand until the plasma pressure equilibrates the back pressure from the ambient gas.^{6–9} The presence of ambient gas during plasma expansion also leads to ambient gas excitation and ionization; however, a controversy exists on the mechanism leading to ambient gas excitation and ionization. The prominent explanations mentioned in the literature are prompt electron excitation and ionization,^{6,10} photoexcitation by high energy photons emitted by the plasma (UV, DUV, etc.),^{7,11} and shock wave heating.¹²

There are three possible mechanisms that explain plasma expansion due to absorption of incident laser radiation after generation of the spark: hydrodynamic, radiative, and breakdown mechanisms.¹³ Initially, a small absorbing layer of gas is excited by laser irradiation leading to ionization and generation of a plasma. A shock wave will be generated in the gas medium at the same time and propagates in the undisturbed gas in all directions. The gas in the shock wave is heated and ionized, creating an optically thick region that absorbs incoming laser radiation, and hence the absorption region moves towards the incoming laser direction. This hydrodynamic phenomenon is similar to detonation of explosive materials and is commonly called the laser-supported detonation wave (LSDW). In the second mechanism, the emitted radiation from the plasma heats the adjacent gas layer, which in turn ionizes and becomes optically thick. In this scenario, the energy is transported by radiation rather than hydrodynamic motion and hence is named as the laser-supported radiation wave (LSRW), which propagates towards the laser beam.

^{a)}hari@pnnl.gov

The propagation of this quasi-steady state radiation wave towards the laser beam generates nearly uniform plasma conditions behind it. In the third scenario, the breakdown occurs along the channel of laser focusing beams, typically happens with the use of a long focal length lens, and is called a laser-supported breakdown wave (LSBW).

Laser-generated air breakdown plasmas characteristically radiate intense continuum radiation, followed in time by ionic, atomic, and molecular emission. When the temperatures of air plasmas reach $>1\text{--}2\text{ eV}$, the molecules in the air are dissociated to atoms and ions.^{14–16} The hot core of the air plasmas are typically heated to $2\text{--}5\text{ eV}$ and generate excited atomic and ionic species (N^* , O^* , C^* , N^+ , O^+ , C^+), while excited molecular species (N_2^* , N_2^+ , OH^*) are typically assumed to be formed during spark cooling.^{14,15} However, the generation of molecular excitation and emission could also occur through other mechanisms. One possible mechanism is heating of the ambient gas and corresponding excitation of molecular species by the shock wave propagating outward from the laser breakdown. A second mechanism is excitation of the surrounding medium via UV radiation produced by the spark. While many studies have examined spectral emission from the core, or kernel, of the air spark, to the authors' knowledge; no studies have investigated emission from the surrounding ambient gas.

The aim of this work is to understand the entire lifecycle of spark generation, expansion, and collapse, and in particular, to differentiate the various mechanisms leading to atomic and molecular emission from the air spark. Such a comprehensive study has not to our knowledge been presented in the literature. Multiple plasma diagnostic tools are used in this study to evaluate the evolution of laser generated sparks throughout their lifetimes. Focused shadowgraphy with high magnification is used for investigating the internal structures in the spark at the early times, while lower magnified shadows are used for evaluating the shock and turbulence mixing at later times. The shock and hot core features obtained from the shadowgraphy results are compared with spectrally integrated fast gated imaging, while molecular and atomic emission features are investigated using time and space resolved emission spectroscopy. In particular, we spatially resolve the emission from the plasma core and the surrounding ambient gas to determine the different excited species in these regions. Based on the measured results, we show that the ambient gas surrounding the plasma core is initially heated by UV radiation to excite and dissociate molecular species, and that the shock wave provides a secondary heating of these regions.

II. EXPERIMENTAL DETAILS

Laser breakdown plasmas were generated in open laboratory air using 1064 nm pulses from a Q-switched Nd:YAG laser (Continuum Surelite II) with a duration $\sim 6\text{ ns}$ full width at half maximum (FWHM). The pulse energy from the laser was varied by using a half wave plate and a cube beam splitter. To generate the air spark, the laser pulses were focused using an f/5 anti-reflection coated aspheric lens. A 200 ps rise time photodiode was used to record the temporal

profiles of the incoming and transmitted laser pulse through the focal volume. The temporal profiles were monitored using a 1 GHz bandwidth oscilloscope.

We used a focused shadowgraphy set up to record shadowgrams. In this set up, a relay lens was used to image the plasma plume onto a CMOS CCD detector. To record the lifecycle of the spark at different time windows with excellent spatial precision, the magnification of the shadowgram image was varied by using various optics combinations for imaging. For probing, a frequency doubled Nd:YAG laser (Continuum Surelite EX) at 532 nm and a pulse duration of $\sim 4\text{ ns}$ FWHM were used. The probe laser was synchronized with the spark-generating laser using two digital delay generators with a maximum temporal jitter of $\leq 1\text{ ns}$. A synchronized CCD camera captured the resulting shadowgram of the laser spark. The delay between pump and probe lasers and the camera were varied to interrogate the plasma plume at different times during its expansion. Fast photography was accomplished with an intensified CCD (ICCD, Andor, iStar) camera placed orthogonal to the laser beam. An objective lens (Canon Macrolens, $f=70\text{--}210\text{ mm}$) was used to image the spark region onto the camera. The visible radiation from the spark was spectrally integrated over the wavelength range of 350–900 nm.

A 0.5 m triple grating spectrograph (Acton, SP2500i) was used for recording the spectral details from the air spark. An optical system was used to image the spark onto the entrance slit of the spectrograph so as to have a one-to-one correspondence with the sampled area of the spark and the image. For collecting the spectral emission features of the spark kernel as well as the UV/shock induced heating and excitation of cold air, the spark plume was imaged onto the spectrograph slit along the laser focusing direction. For light detection, the spectrograph was equipped with two detectors: an intensified charged coupled device (ICCD, Princeton Instruments, PiMAX) and a photomultiplier tube (PMT, Hamamatsu R928). A diverting mirror was used to change the dispersed light path to the ICCD or PMT detectors. The spectrograph in conjunction with the ICCD was used to record the spectral details of the spark at various distances from the kernel, while the monochromator-PMT combination was used to study the temporal evolution of various excited species in and around the spark volume.

III. RESULTS AND DISCUSSION

There are numerous studies focused on laser breakdown threshold of air at atmospheric pressure and reported values are in the range $\sim 6 \times 10^{11}\text{--}3 \times 10^{12}\text{ W/cm}^2$ depending on the irradiation conditions.^{17,18} The temporal profiles of the laser pulse used for the air spark generation and the transmitted laser pulse propagated through the spark are given in Fig. 1 for a pulse energy of 55 mJ. The focused laser energy, which is significantly higher than the breakdown threshold of air, generates a plasma column in air with a length (along the laser propagation direction) $\sim 2\text{ mm}$. The starting point of breakdown (breakdown threshold) depends strongly on the laser focal conditions,¹⁹ laser wavelength,²⁰ pulse duration,¹⁷ and ambient gas pressure.²¹ Since the energy absorption

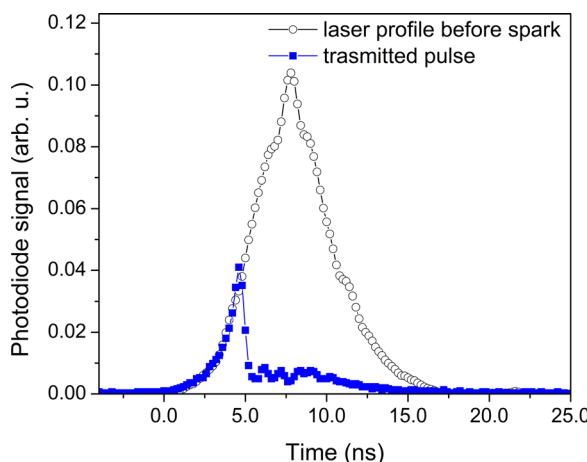


FIG. 1. The temporal profile of the laser pulse used for generating the spark is given along with the recorded transmitted pulse through the spark.

process begins only when the laser energy exceeds the breakdown threshold value, the leading edge of the pulse below the breakdown threshold is transmitted unperturbed into and through the focal region. As the power increases, laser-supported absorption waves are formed and the spark begins to absorb more energy after the breakdown event. The significant energy absorption by the plasma above the breakdown threshold indicates inverse bremsstrahlung is important in subsequent heating and ionization of the plasma. When the laser energy is well above the breakdown threshold, more than 85% of the energy will be consumed by the spark.^{21–23} It can be seen in Fig. 1 that a small percentage of the laser energy is transmitted even after generation of the spark. Since plasma formation has a negative contribution to the refractive index, causing defocusing of the incoming laser beam, a small part of the trailing edge of the laser pulse is transmitted.

A. Shock wave propagation

We used focused shadowgraphy to record the shock waves generated by the air spark, which monitors the spatial variation of refractive index across a probe beam. The main advantage of using focused shadowgraphy is that it allows variable magnification of the recorded shadowgram. Such variable magnification shadowgraphy systems are useful for

visualizing the transient internal structures of shockwaves generated at early times and for capturing turbulent mixing at later times in the spark lifecycle. In the present study, different magnifications were used for capturing shadowgrams at early (0–60 ns), mid (0.1–1.5 μ s), and late times (1 μ s–2 ms) of the air spark lifecycle. Fig. 2 gives a series of shadowgram images recorded at early and mid times of the spark lifecycle, illustrating the spatial and temporal evolution of the air spark. The laser energy used was \sim 55 mJ and the time given in the figure begins after the onset of plasma formation. Each frame is recorded from different laser shots and based on the images given it can be concluded that the shadowgrams are highly reproducible.

Although the boundary of the discontinuity in refractive index is very evident at all frames shown in Fig. 2, the shadow images recorded at earlier times and during the laser pulse (\leq 10 ns) showed elongated darkened regions with blurring on the side closest to the focal lens. The presence of this darkened regime at earlier times could be due to high densities of plasma radiation at early times and/or lack of temporal resolution caused by the long probe laser pulse width (\sim 4 ns FWHM) relative to kernel expansion. It has to be pointed out that even if the plasma density is lower than the critical density of the probe beam (which is \sim 4 \times 10²¹/cm³); at high plasma densities, the free-free absorption can attenuate the probe beam. The formation of an elongated plasma column at early times was previously explained as being due to translation absorption.^{24,25} The absence of a clear boundary in the backward direction during the laser pulse could also be due to rapid changes in the laser absorption zone position. Due to rapid changes in the laser absorption zone, the density and pressure fields are irregular for the spark during the laser pulse, leading to an extremely complex flow field.

Typically, the LSBW is prevalent when a longer focal length lens is used for generating laser breakdown plasma.^{23,26} However, its role is limited in the present experiment with the use of a relatively short focal length lens ($f = 5$ cm) for focusing the incoming laser beam. Hence for short focal length lens focusing, the velocity of the laser spark along the incoming laser direction is determined by the faster of the two mechanisms (LSDW and LSRW); however, the transition between these two is not fully understood,

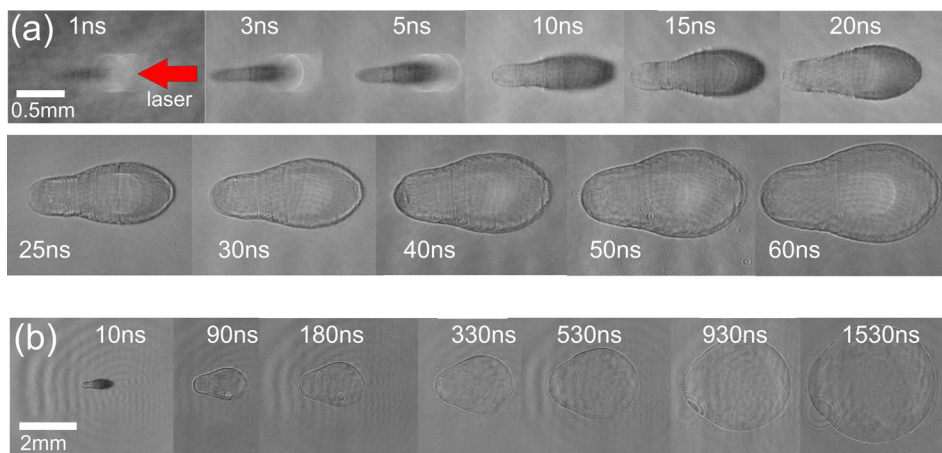


FIG. 2. Shadowgrams taken at different times during the evolution of the air spark obtained using (a) higher magnification and (b) low magnification. The times given in the figure correspond to the times after the onset of plasma generation.

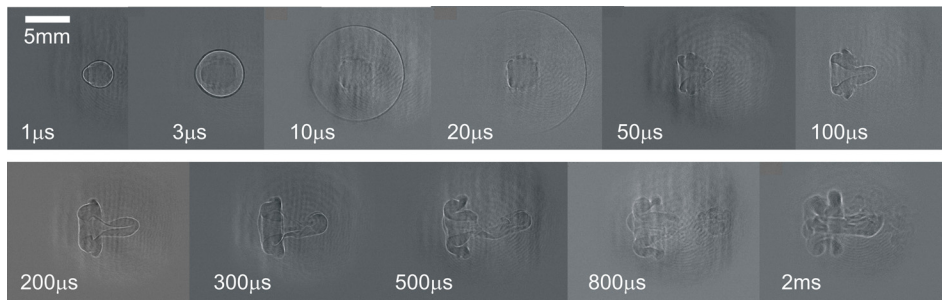


FIG. 3. Shadowgrams taken at later times of spark lifecycle.

considering that the dynamic and radiation mechanisms propagate with approximately similar wave velocities. Yalcin *et al.*²⁷ used similar experimental conditions as in our experiments and the growth of plasma was well described by a LSDW; Bergel'son *et al.*²⁸ described the conditions of LSRW using a simple model.

At early times, striations are seen in a direction orthogonal to LSDW/LSRW propagation. Typically striations are commonly seen when instabilities are present in the plasma jets.^{29,30} The observation of internal grooves or striations can be seen even at the first frame (~ 1 ns). The structures of the shock wave at the moment of breakdown have been reported by many researchers, but the mechanisms leading to the formation of such structures are still not clear.^{31–33} Even though a relatively short focal length lens ($f = 5$ cm, Rayleigh length $\sim 135 \mu\text{m}$) is used for the present studies, the possibility of formation of a LSBW is still possible considering the long Rayleigh length compared to the focal spot size of $\sim 10 \mu\text{m}$, indicating that multiple sparks may be formed during translation absorption^{24,25} at the earliest times of the spark's evolution. Also please note that at the earliest times (≤ 5 ns), the morphology of the spark is cylindrical. It has to be pointed out that for the cylindrically symmetric plasma column, as observed during the laser pulse, the refraction of the probe laser light is greatest near the outer edge of the plasma, i.e., where the radial electron density gradients are perpendicular to the ray's path and where the ray's path through the plasma is longest. Such gradients can appear as vertical striations in the shadowgram images too.³⁴

From Fig. 2, the shock fronts can easily be seen in the shadowgrams at times ≥ 10 ns. As time evolved, a LSDW/LSRW was formed and moved towards the laser beam with a higher velocity compared to its counterpart in the opposite direction. Hence during the later phases of the laser pulse and at the beginning of the adiabatic regime, the spark possessed an asymmetric spherical dumbbell shape. This can be understood by considering the imbalance in laser deposition. After the generation of the spark, the rest of the laser energy is absorbed by the LSDW/LSRW, which moves towards the incoming laser beam. The shadowgrams recorded during the midlife of the spark (Fig. 2(b)) show that the asymmetry and ellipticity observed at earlier times disappear when the shock front expands into the surrounding cold undisturbed air. Fig. 3 shows the shadowgrams obtained at later times (up to 2 ms) of the spark lifecycle. Please note the changes in magnification in the shadowgram images given in Figs. 2 and 3. The shock waves approach a spherical shape at times $> 3 \mu\text{s}$ and disappear out of the field of the imaging region at later

times ($t \geq 20 \mu\text{s}$). The decoupling of the shockwave from the plasma core can also be seen at times $t > 1 \mu\text{s}$. It indicates that the plasma and shock waves expand with similar velocities until $t \sim 1 \mu\text{s}$. Though the expanding shock showed spherical symmetry at times $> 3 \mu\text{s}$, the detached hot core became asymmetric after the decoupling, and further deformed with time before eventually collapsing inward opposite to the laser propagation direction. At times $> 50 \mu\text{s}$, the mixing of the hot and cold air is evident, denoted by the appearance of a vortex ring resulting from the initial non-spherical shock wave.^{35–38} At these times, turbulence begins to dominate.

The shadowgram sequence of images show the shock front propagates very rapidly at the earliest times and slows down at later times. The expansion of an air spark system in which a great amount of energy is released in a point was treated by the self-similar flow.³⁹ The position-time ($R-t$) plot obtained from the shadowgram is given in Figure 4 along with estimated velocity. We compared the $R-t$ data with Taylor-Sedov theory,³⁹ which states that the blast wave propagation from a point explosion follows:

$$R = \xi \left(\frac{E}{\rho_b} \right)^{\frac{1}{n+2}} t^{\frac{n-2}{n+2}},$$

where t is the delay time following ignition, ρ_b is the background gas density, E is the amount of energy released during the explosion, and ξ is a constant, which depends on the

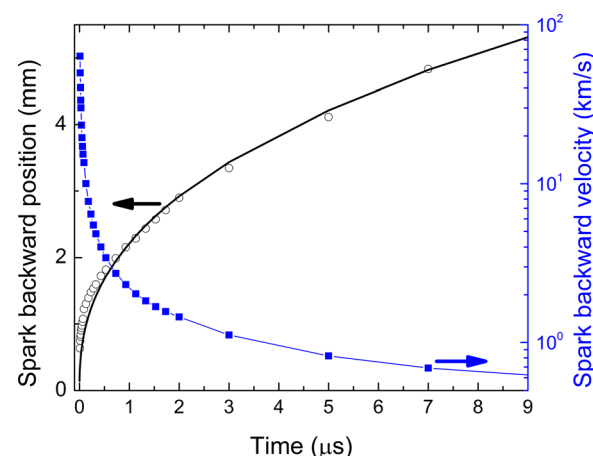


FIG. 4. The spark front position towards the laser direction with time is given in the left y-axis (circles). The smooth line corresponds to a Taylor-Sedov fit. The estimated spark velocity in the laser direction is given in the right y-axis (squares).

specific heat capacity ratio. The value of $n = 3, 2$, or 1 represent spherical, cylindrical, or plane wave shock wave propagation, respectively. According to Taylor,⁴⁰ the blast wave consumes approximately two thirds of its source energy. Figure 4 (solid black line) shows a fit to the measured data assuming a spherical blast wave in which R is proportional to $t^{2/5}$, which shows good agreement with the recorded spark expansion behavior, especially at later times. The deviation from the blast wave at the early times can be understood considering the near cylindrical shape and expansion of the spark at early times caused by translational absorption combined with LSDW/LSRW expansion. The velocity data show that the spark expands rapidly in the first few 10's of nanoseconds. High hypersonic shock velocities (> 25 km/s) are seen during this time caused by laser propagation waves; however, it slows to near-hypersonic velocities within 500 ns. Supersonic velocities are obtained at ~ 700 ns and the shock moves to sonic velocities at $\sim 5 \mu\text{s}$. According to the shock wave model,³⁹ the end of shock expansion occurs when the pressure of the shock front equates the pressure of the medium.

According to Zeldovich and Raizer,³⁹ the pressure of the shock wave and the temperature behind the shock wave are proportional to the square of the velocity for gases such as air with a constant specific heat. Fig. 5 shows the pressure and temperature decay based on measured velocities of the air spark for the backward shock.³⁹ The temperature behind the shock front approaches a value of $\sim 5 \text{ eV}$ at 30 ns after the onset of spark formation and decays rapidly with time to reach $\sim 0.1 \text{ eV}$ at $\sim 1 \mu\text{s}$. The estimated shock pressure also showed a similar trend. At early times ~ 30 ns, the shock pressure is extremely high (≥ 500 atm) and it drops to 10 atm at $t \sim 1.1 \mu\text{s}$. The shock pressure approaches atmospheric levels at times $> 20 \mu\text{s}$. We noticed the formation of turbulence mixing above these pressure levels as seen in the shadowgraphic images (Fig. 3), which happens when cold air squeezes through the weak shock wave to mix with the hot air in the region behind the shock wave.

The present results employing focused shadowgraphy with varying magnifications enabled visualization of the transient nature of spark generation, internal structures, asymmetric expansion, shock wave decoupling from the hot

core and turbulence. The shadowgraphic images showed that the spark possesses a cylindrical shape at early times ($\leq 1 \mu\text{s}$), which is caused by preferential absorption of the incoming laser beam by the spark front facing the beam, followed by a spherical shape at midlife ($\sim 3-20 \mu\text{s}$) and formation of turbulent structures at the end of the lifecycle. However, even though the shadowgrams reveal inhomogeneities in the refractive variation in the spark medium during its lifecycle, the emission from the spark will not necessarily show similar structures to those seen in the shadowgrams. The amount of emission depends on the local temperature and spectroscopic composition, while the transmission of the shadowgram probe beam depends more on the local density and its absorption properties. Hence a comparison of shadowgram images with self-emission from the kernel provides more insight into the spark lifecycle and will be presented next.

B. Plasma self-emission dynamics

The time evolution of spark self-emission was studied using fast-gated photography employing an ICCD. The images are taken such that the ICCD camera views the self-emission from the spark orthogonal to the laser propagation direction. Fig. 6 gives the evolution of the air spark at various times after the onset of spark generation. A 2 ns gate width was used to record the images at early times up to 1000 ns, while a 10% gate width with respect to the delay time was used at later times to compensate for the reduction in emission intensity. The laser energy used was 55 mJ and each image in the figure is recorded from an independent breakdown event and normalized to its maximum intensity. The laser beam is incident from the right hand side (indicated in the first frame). Similar to the shadowgraphic image sequence, the smoothness of the spark evolution attests to the reproducibility of the data. The shape of the air spark at early times is found to be spherical. This is contrary to the shadowgram images, where an elongated channel is seen. With time, the spark image becomes more asymmetrical in shape; the backward plasma (towards the focusing lens) grows much faster than the forward plasma.

The internal structures seen in the shadowgram images (Fig. 2(a)) at early times are found to be absent in the self-emission images (Fig. 6). The shadowgram gives the second derivative of the refractive variation, which will reveal inhomogeneity in the medium of interest; the self-emission recorded from the spark fireball is very intense at early times, and capturing such inhomogeneity requires a faster gating time than the one used (~ 2 ns) in the present studies. Previous reports showed the presence of internal structures in the self-emission spark image with the use of a long focal length lens.^{23,26,41} In that scenario, the LSBW is predominant during the laser pulse. Similar to the shadowgraphy images, the spark morphology obtained by recording self-emission also reveals significant changes with time. The asymmetrical dumbbell-shaped spark observed at early times ($t \leq 200$ ns) gradually changed into a triangular shape at $t \sim 4 \mu\text{s}$. This process coincides with the detachment of the shockwave from the hot core and further deformation

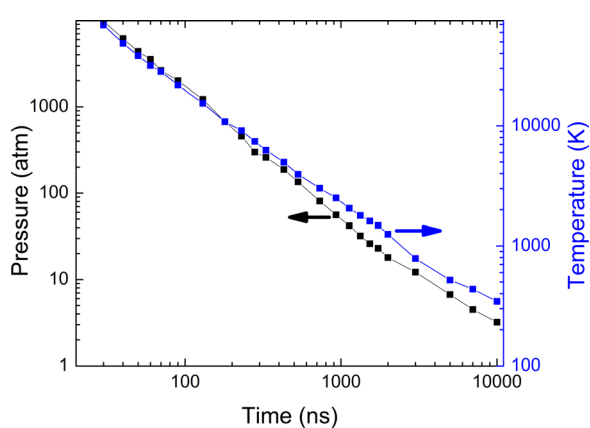


FIG. 5. The spark shock pressure and the temperature behind the shock wave are given. The values are tabulated from Zeldovich and Raizer.³⁹

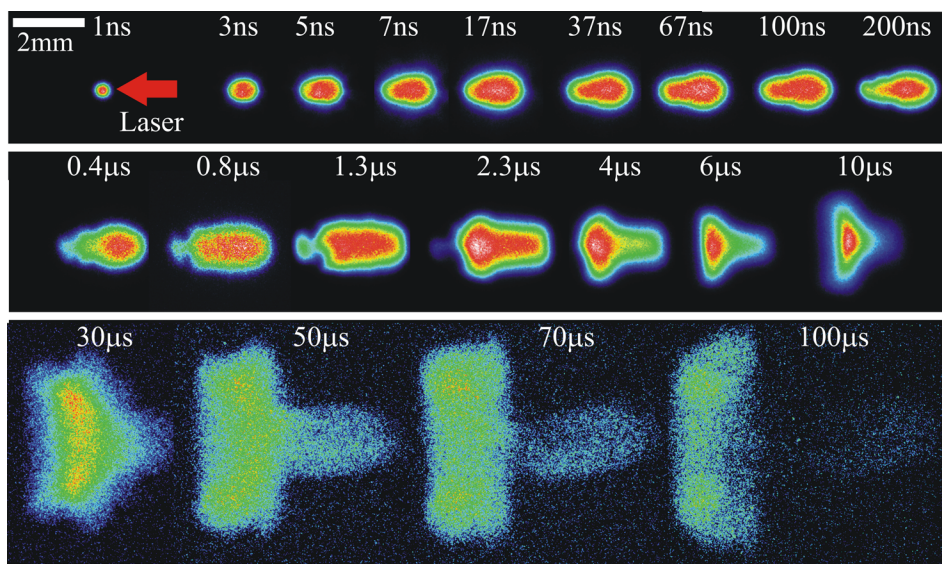


FIG. 6. The time evolution of spectrally integrated visible emission in the wavelength range 350–900 nm from the air spark recorded using an ICCD camera. The laser energy used was 55 mJ. The timings in the images represent the time after the onset of spark formation. All images given are normalized to their maximum intensity.

noticed with time in the shadowgram images. The internal structures seen at later times of the self-emission images are also found to be complimentary to turbulent structures noticed in the shadowgram at later times. This also indicates that the spark is still emitting light in the turbulent regime.

The position-time plot obtained from the ICCD sequence of images is given in Fig. 7. The laser-supported wave is found to move extremely fast with an estimated velocity $\sim 100 \pm 5$ km/s during the laser pulse and slows down immediately after the end of the pulse. During the laser pulse and after the termination of the laser pulse, the spark expansion is found to be higher in the backward and orthogonal directions (see Figure 6). The spark backward position noticed using the ICCD showed a somewhat different trend compared to shock position observed using shadowgraphy even though the shadowgram images showed the decoupling of the shock and plasma happen only at times $\sim 1\ \mu\text{s}$. For example, the self-emission images showed the plasma propagated to ~ 1.25 mm at the end of the laser pulse ($\sim 10\ \text{ns}$), while the shadowgram images showed the shock wave took

$\sim 100\ \text{ns}$ to reach this distance. To explain this difference, we note that the UV radiation emitted by the spark may dissociate, excite and/or ionize the ambient medium, leading to emission from regions outside the initial kernel of the spark; therefore, the self-emission images at early times do not necessarily represent the spark boundaries. However, at later times ($>100\ \text{ns}$), the shock waves seen in the shadowgrams are found to move faster compared to self-emission images recorded using the ICCD. This implies that the outer regions of the spark are not emitting strongly at later times, possibly caused by rapid cooling of the plasma by cold ambient gas at the plasma-ambient interface or relaxation of UV heated areas.

The shadowgram and self-emission images showed significant differences in the propagation (in the backward direction, Fig. 7) as well as in the morphology during the laser pulse (elongated vs circular). However, based on Figs. 2(a) and 6, the spark morphology showed reasonable similarities at times $\sim 10\text{--}100\ \text{ns}$. For a direct comparison between shadowgram and self-emission images from the spark plasma, the images obtained at various times using these two diagnostic tools are given together in Fig. 8. At early times ($\sim 100\ \text{ns}$), the length and shape of the spark column is found to be approximately similar for both cases. However, the shapes showed a marked difference in the mid lifecycle of the air spark. For example, at $t \sim 0.5\ \mu\text{s}$, the self-emission images showed most intense radiation along the optical axis, where the temperature is expected to be maximum; however, the shadowgram showed a more circular shape. The geometry of the spark emission showed a triangular shape after decoupling of the shock wave from the hot core. It can be assumed that after decoupling of the shock front from the plume, the reflected shock wave propagates rapidly back toward the spark plume, thereby halting further expansion of the plasma. Recent atomistic modeling results show that spatial confinement of the plume by shock wall reflection leads to an increase in local temperature and emission lifetime.⁴² Hence we believe that the triangular shape of the self-emission image during the spark's midlife could be caused by plasma adiabatic compression.

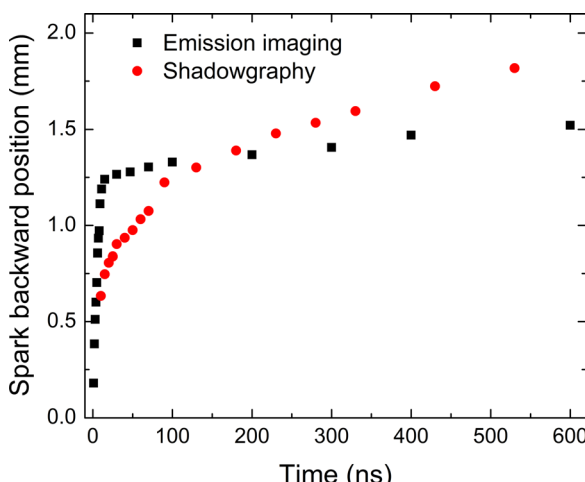
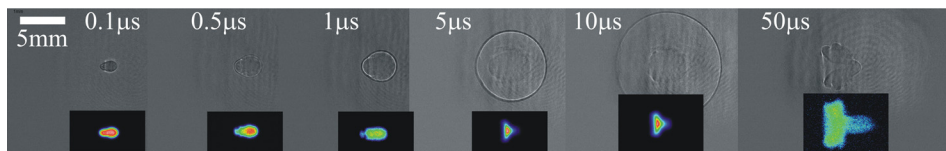


FIG. 7. The position-time plot obtained from ICCD images is given. For comparison purpose, the data obtained from shadowgraphy is also provided.



Recently, Aguilera and Aragon⁴³ studied the evolution of temperature and density of air sparks generated under similar conditions used in the present studies (1064 nm excitation, ~ 5 ns FWHM, ~ 60 mJ) and found temperature and density reach $\sim 50 \times 10^4$ K and $5 \times 10^{17}/\text{cm}^3$ at the earliest times and decay rapidly during the initial expansion phase ($\leq 1 \mu\text{s}$). However, the spark parameter changes are found to be minimal during the midlife (1–6 μs) of its expansion. The reduction in the rate of change of spark parameters during this time can be correlated to plasma decoupling from the shockwaves and subsequent suppression of the core region expansion, which stabilizes the temperature and increases the emission lifetime. This is also consistent with recent numerical simulations of a decaying air spark, which showed two temporal phases; in the first phase rapid changes in the flow and physical parameters occur where convection and radiation are the dominant heat transfer mechanisms, while in the second phase changes become much slower and regular where conduction is the major heat transfer mechanism.³⁸ At later times, $t \geq 10 \mu\text{s}$, the plume is again found to expand and the spark and shadowgram turbulent features show good similarity.

Although shadowgram and fast-gated emission images have shown morphological analogy at earlier and late times, it is not clear from the images that the shock waves are exciting and/or ionizing the ambient medium. This could be partly due to the fact that the dynamic range of the ICCD is not high enough to record the potentially weak emission from these regions. It has to be mentioned that the spark shock parameters: *viz.* velocity, pressure, temperature as well as spark volume are strongly dependent on the heating laser pulse energy. Fig. 9 shows the recorded shadowgrams and self-emission images for the air spark at two times (100 ns and 500 ns) for various laser energies used (7 mJ, 23 mJ, 73 mJ and 210 mJ). The asymmetry in the spark morphology is found to be higher with increasing laser energies. The asymmetry with increasing laser energy can be related to increased laser absorption by the spark in the laser entering direction. The spatial extension of the shock wave also scales with laser energy: the higher the laser energy the farther the location of the shock front from the focal position, with a more pronounced effect in the backward direction. The volume of the spark also increases with laser energy considerably. For example, at 500 ns the estimated spark volume for 7 mJ and 210 mJ laser energies are 1.64 mm^3 and 26.9 mm^3 , respectively. Previous studies showed negligible changes in the temperature and density of the spark with respect to laser energy.²⁷ This indicates that an increase in laser energy leads to changes in the plasma volume due to preferential laser absorption in the spark front position facing the beam instead of reheating the plasma as a whole, which typically happens in the case of laser coupling to the plasma formed from a solid target.

FIG. 8. The shadowgrams and ICCD images are shown together. The spatial scale is approximately the same for all images.

C. Spectral characterization of plasma

The fast-gated self-emission and shadowgraphy images provide details of expansion and transient morphological changes in the air spark; however, they provide limited information regarding the various physical and chemical processes happening in the spark kernel and surrounding medium. The laser energy dependence study showed significant propagation of shock waves in the backward direction and good similarity in the shadowgram and self-emission images at two moments of its lifecycle. However, the roles of shock waves, UV radiation, and/or fast electrons from the spark on dissociation and subsequent excitation of the ambient medium is not clear. Therefore, we utilized space- and time-resolved spectroscopy to evaluate various excitation mechanisms leading to emission from the spark and from the surrounding cold medium.

The early time spectral features of air spark kernel are well-studied and available in the literature,^{20,21,27,43,44} while our aim in this paper is to evaluate the various mechanisms leading to dissociation, excitation, and ionization in a laser-created air spark during its entire lifecycle. In addition, most of the previous spectroscopic studies of air sparks were either spatially integrated or “line of sight” averaged orthogonal to the spark expansion direction.^{15,16,20,21,44} This set up

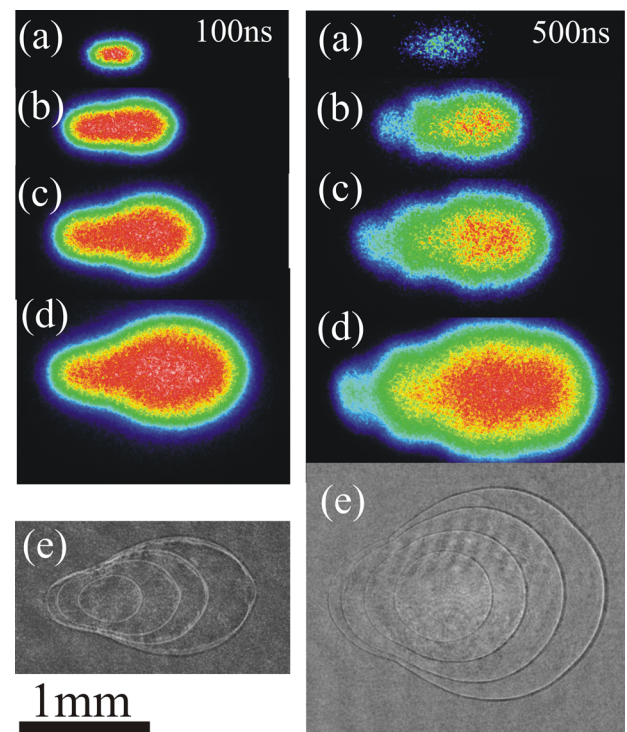


FIG. 9. Shadowgram and self-emission images recorded at (left) 100 ns and (right) 500 ns for various energy levels ((a) 7 mJ, (b) 23 mJ, (c) 73 mJ, and (d) 210 mJ). The images in the shadowgram (e) show all laser energy levels with larger size corresponding to higher laser energies.

does not differentiate the details of emission features from the kernel and the surrounding region, due to UV and/or shock dissociation/excitation of the ambient medium. In order to overcome these issues, we imaged the spark onto the spectrograph slit in such a way that the slit height is along the spark/laser propagation direction (see inset in Fig. 10(a)). In addition, the emission features of the air spark are recorded at different times in the lifecycle. By recording spectra at various distances from the laser propagating axis and at various times after spark formation, we believe that differentiation between the emission features provided by the various excitation mechanisms is improved.

Typical spectra recorded at various distances from the spark kernel (0 mm, 1.25 mm, 2.5 mm) are given in Fig. 10 at times 10 ns, 100 ns, 1 μ s, and 10 μ s after the generation of the air spark. The inset in Fig. 10(A) gives the recording

positions (slit location with respect to air spark). The spectra were recorded with a 300 grooves/mm grating with a dispersion in the detector plane of ~ 7 nm/mm. In order to compensate for the reduction in intensity at later times after spark formation, the gating times used are different at various locations and delays. Details of the gate delays, gate widths, number of spectral accumulations, and spectrograph slit widths for each distance and time are given in Fig. 10.

At 0 mm, the early time spectrum (~ 10 ns) showed continuum emission resulting from bremsstrahlung, which indicates a highly ionized plasma. The spectrum recorded at ~ 100 ns showed significant line emission contributed mainly by N II superimposed with continuum radiation. The prominent N II lines observed include 343.7 nm, 399.5 nm, 444.7 nm, 463.1 nm, 500.5 nm, 571.1 nm, and 592.7 nm. A weak signature of O I (~ 777 nm) and N I (~ 744 nm) can

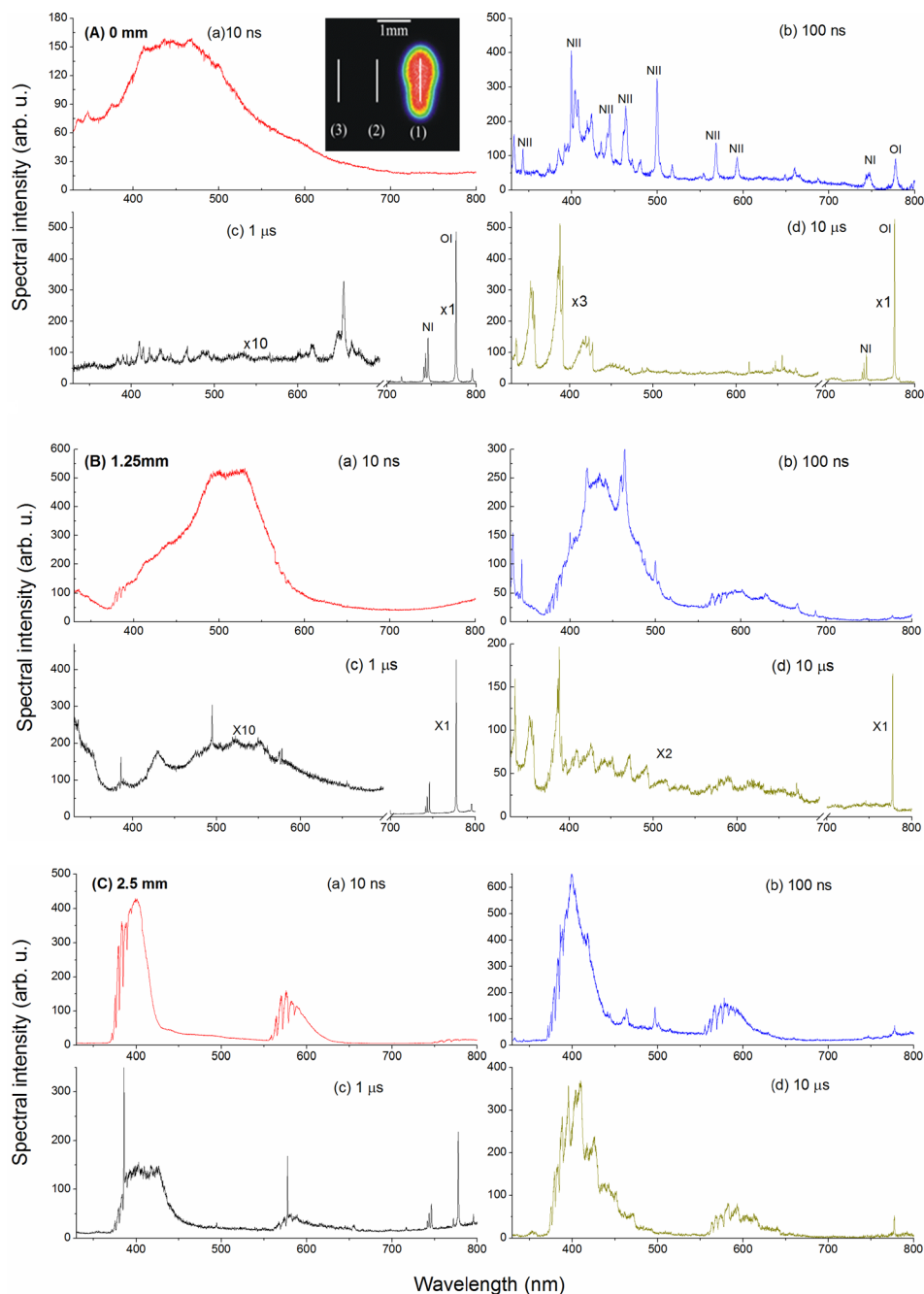


FIG. 10. The spectral details of the air spark recorded at various distances and times after the onset are given. The laser energy used was 55 mJ. The timings in the images represent the time after the onset of spark formation. The inset image given in (A) represents the spectrograph slit (sampling) positions used with respect to the plasma kernel (1 corresponds to 0 mm, 2 and 3 slit positions represent 1.25 and 2.5 mm, respectively). The gate delays (τ_d) and gate widths (τ_w) used for each spectral frame (τ_d , τ_w) are given below. (A)-(a) (10 ns, 2 ns); (A)-(b) (100 ns, 2 ns); (A)-(c) (1 μ s, 20 ns); and (A)-(d) (10 μ s, 20 μ s). (B)-(a) (10 ns, 10 ns); (B)-(b) (100 ns, 10 ns); (B)-(c) (1 μ s, 100 ns); and (B)-(d) (10 μ s, 20 μ s). (C)-(a) (10 ns, 10 ns); (C)-(b) (100 ns, 100 ns); (C)-(c) (1 μ s, 1 μ s); and (C)-(d) (10 μ s, 20 μ s). The spectra given are accumulated from 25 events. Slit widths used for collecting the spectral features: (A) 10 μ m, (B) 20 μ m, and (C) 30 μ m.

also be seen in this spectrum. At $\sim 1 \mu\text{s}$, weak molecular bands are seen mixed with intense atomic line emission. The most intense atomic lines among them are O I ($\sim 777 \text{ nm}$) and N I ($\sim 744 \text{ nm}$). The O I and N I line widths are also found to be significantly narrower at $1 \mu\text{s}$, indicating a reduction in electron density. At 0 mm and at $10 \mu\text{s}$, the measured spectrum is dominated by molecular bands. Similar molecular band emission features from atmospheric pressure air plasmas have been reported.^{15,16,45}

For the emission spectrum acquired at 0 mm and at a gate delay of $10 \mu\text{s}$, assignment of the dominant emission features in the air-spark kernel were aided by comparison of the experimental spectrum to a simulated emission spectrum using SPECAIR.⁴⁶ This comparison is shown in Fig. 11. To match the width of the spectral features observed in the experimental spectrum, it was necessary to account for instrumental broadening, indicating that the electron density is low enough by $10 \mu\text{s}$ that Stark broadening is a minor contributor to the observed spectral linewidth. The simulated emission spectra have been convolved with a Lorentzian slit function to account for this instrumental broadening. Based on the spectral simulation, the atomic emission is dominated by O I ($\sim 777 \text{ nm}$) and N I ($\sim 744 \text{ nm}$), while the molecular emission is dominated by N_2^+ and CN. Assuming local thermodynamic equilibrium (LTE), the spectral simulation was generated using a temperature of 7000 K that was found through fitting of the emission bands belonging to N_2^+ (B-X), and CN (B-X) observed from 360 nm to 475 nm along with weak emission from N_2 (C-B and B-A). Given the $20 \mu\text{s}$ gate width, this is a time-averaged estimate of the plasma temperature. Overall, the correspondence between the experimental and simulated spectrum is excellent for the dominant emission features from O I, N I, N_2^+ , N_2 , and CN.

Spectral information recorded at various distances from the plasma kernel provides valuable insights for differentiating various excitation mechanisms leading to emission from atomic and molecular species. Typical spectra obtained at 1.25 mm and 2.5 mm away from the plasma kernel mid-plane are given in Figs. 10(B) and 10(C). Again, the inset in Fig. 10(A) gives the details of the sampling positions used for measuring the spectra with respect to the plasma kernel. According to the shadowgram images given in Figs. 2 and 3, the shock wave takes approximately $\sim 500 \text{ ns}$ and $2 \mu\text{s}$ for reaching observation positions of 1.25 nm and 2.5 mm, respectively. Therefore, for the spectra given in Figs. 10(B) and 10(C), it can be concluded that the early time emission features recorded at both 10 ns and 100 ns delays are solely due to UV and/or fast electron excitation of the cold air medium and not heating by the propagating shock wave.

Excitation and ionization of surrounding ambient medium at early time before the arrival of plasma has been reported previously for laser-solid target interaction and explained by the prompt electrons and/or photoionization.^{6,7,10,47} Laser generated plasmas are a good source of high energy photons and currently they are being proposed for EUV sources for lithography⁴⁸ and water-window sources for microscopy.⁴⁹ There exists, however, some controversy on the mechanisms leading to excitation and ionization of the ambient medium during laser plasma generation. For example, Amoruso *et al.*¹⁰ observed highly energetic prompt electrons using an electrostatic energy analyzer (EEA) during 248 nm laser ablation of an Al target and explained that the prompt electrons are generated due to two photon photoelectric effects during the laser pulse. A similar kinetic distribution of fast electrons was observed by Issac *et al.*⁶ during Nd:YAG laser ablation of Ag leading to excitation and ionization of the ambient medium. Cronberg *et al.*⁵⁰ suggested

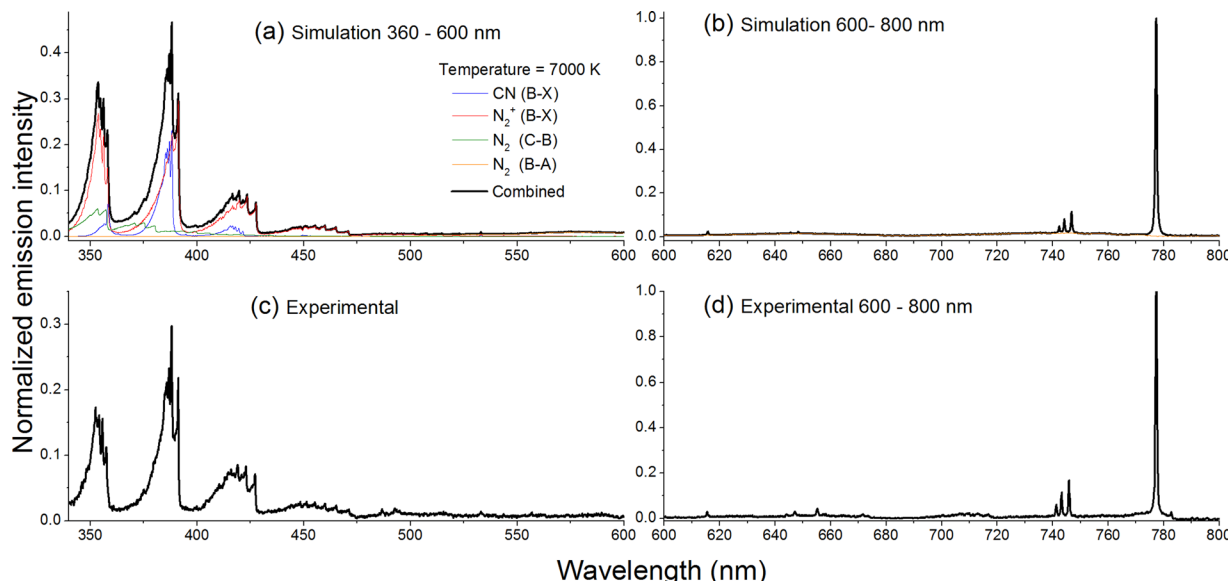


FIG. 11. A comparison between simulated emission spectra using SPECAIR and the experimental emission spectrum collected from the air spark kernel (Fig. 10(A) panel (d)). (a) and (b) present the simulated emission spectrum at a temperature of 7000 K in the spectral region 360–600 nm and 600–800 nm, respectively. In panel (a), the individual emission intensity contributions from CN, N_2 , and N_2^+ are shown as individual traces. Panels (c) and (d) present the corresponding regions from the experimental emission spectra. The intensities in the experimental spectra were first normalized using a spectral efficiency curve of the grating and detector, followed by normalization to the peak intensity of the O I atomic emission feature at 777 nm.

that the origin of the high kinetic energies was due to collisional inverse bremsstrahlung absorption experienced by photo emitted electrons. Recently, Ratynskaia *et al.*⁷ argued that prompt electrons require energies in excess of 1 keV for exciting and ionizing nitrogen ambient and generation of such high energy electrons are not possible with low-energy ns laser-matter interaction and hence photoionization is the major mechanism for ambient excitation and ionization. However, it has to be mentioned that all above measurements were performed at low pressures (\sim mTorr) and the attenuation of high energy photons and prompt electrons will be increased with enlarged background pressure levels. Moreover, in the present experiments, the plasma kernel was produced by focusing laser photons onto an air medium (760 Torr at room temperature), heating of the plasma to very high temperatures (\geq 10 eV) is not expected because of non-localized laser absorption.

Broadband emission dominates the spectrum recorded at 1.25 mm at a 10 ns delay time, although its characteristics are different than the broadband emission at 0 mm. At 100 ns, the broadband emission becomes narrower and atomic and molecular emission lines appear. Weak self-absorption dips or self-reversal is also evident at \sim 380 nm and \sim 570 nm. At a 1 μ s gate delay, the O I and N I lines are the most intense, while at a 10 μ s delay time, the emission spectrum is dominated by molecular bands.

The spectra recorded at various delay times at 2.5 mm showed significant differences compared to the measured spectra at 0 mm and 1.25 mm. First, the broadband emission at 10 ns seen at 0 mm and 1.25 mm is absent at the 2.5 mm distance, indicating a lower overall excitation temperature and ionization degree in this region. The self-absorption at \sim 380 nm and \sim 570 nm appeared at 10 ns for the 2.5 mm distance, which is earlier than for the 1.25 mm distance. However, along with the absorption dips, some emission lines are seen mixed with broadband radiation at 100 ns, especially at a distance 2.5 mm. At 1 μ s, the O I and N I atomic line emission are predominant along with some sharp emission line-like features at 385 nm and 578 nm. The origin of these sharp lines, which are also observed at the 1.25 mm distance, is unknown currently. Molecular emission features are predominant at 10 μ s delay time along with weak O I emission line around 777 nm.

The spectra recorded at various spatial locations during the air spark lifecycle highlight the complex nature of air breakdown. The observed spectra contained broadband emission at early times mixed with absorption from species between the emission and the spectrometer. Atomic and ionic emission features are present at intermediate times, changing to predominantly molecular emission at later times. The recorded spectral features at 0 mm from the plasma kernel showed good agreement with other reported laser air breakdown spectroscopy measurements.^{15,16,20,27} However, the observations away from the plasma kernel at 1.25 mm and 2.5 mm differ substantially from the 0 mm observations. In particular, the broadband-like emission spectra seen at early times deviate significantly from the more typical black-body emission curve seen at 0 mm.

It is expected that the excitation and emission processes are different for the highly excited plasma core and for the surrounding gas. The plasma core is directly excited to a high temperature via absorption of the incident laser pulse, as described above. Regions close to the plasma core may be excited at later times via expansion of the hot plasma region. However, the excitation of the cold air away from the plasma kernel is dictated by UV emission from the core region. Furthermore, the detected emission from these regions is influenced by relaxation and emission of the excited species, and finally transport of the emitted radiation to the spectrometer. Each of these processes involves multiple species at potentially different excitation temperatures, and non-LTE conditions. Also, the emission features from a medium are strongly dependent on the excitation temperatures, and certain lines emit only in small excitation temperature windows.⁴⁵ A detailed explanation of the emission features at various distances from the plasma core, identification of the emitting and absorbing atomic and molecular species, determination of excitation temperatures, and modeling the radiation transport through cold air are beyond the scope of the present work and will be a topic for a future paper.

D. Time resolved studies employing PMT

The space- and time-resolved spectroscopic data clearly show the differences in emission spectra between the plasma kernel and the surrounding cold gas excited by UV emission. To further study and differentiate the effects of UV heating versus shock wave heating on the air surrounding the plasma kernel, we employed time-resolved emission analysis at a fixed wavelength corresponding to an atomic emission line. Such studies provide useful information regarding the formation and time evolution of an emitting species at a particular spatial location. The O I emission line at 777 nm was selected for this study, since it is seen at all distances for times >100 ns. Time-resolved emission was measured using a monochromator tuned to pass a narrow wavelength band near 777 nm, with a PMT as a detector. Typical time-resolved emission traces of the O I 777.2 nm emission line are given in Fig. 12 for various distances from the plasma kernel central position. The sampling distances given in the figure correspond to the distances from the plasma kernel central position (similar to Fig. 10(A) inset).

The temporal evolution of the O I line at 0 mm showed an intense sharp peak followed by a broad temporal emission peak, which persisted beyond 20 μ s. The sharp peak, which appeared at all distances immediately after the laser fired, could be due to broadband emission caused by bremsstrahlung by the plasma kernel at short distances and by UV excitation at larger distances. This is also supported by the fact that O I emission line intensities were not resolved at early times in the recorded spectra shown in Fig. 10. At 0 mm, the O I temporal profile showed a plateau region around 1–4 μ s after the sharp peak at earlier times followed by a peak that showed maximum intensity \sim 6 μ s after the onset of spark formation. The observed delayed O I peak at 0 mm with a delay \sim 6 μ s can be correlated to plasma spatial confinement seen in Fig. 6. With increasing distance from the kernel central plane, the delayed O I peak appears at earlier times and

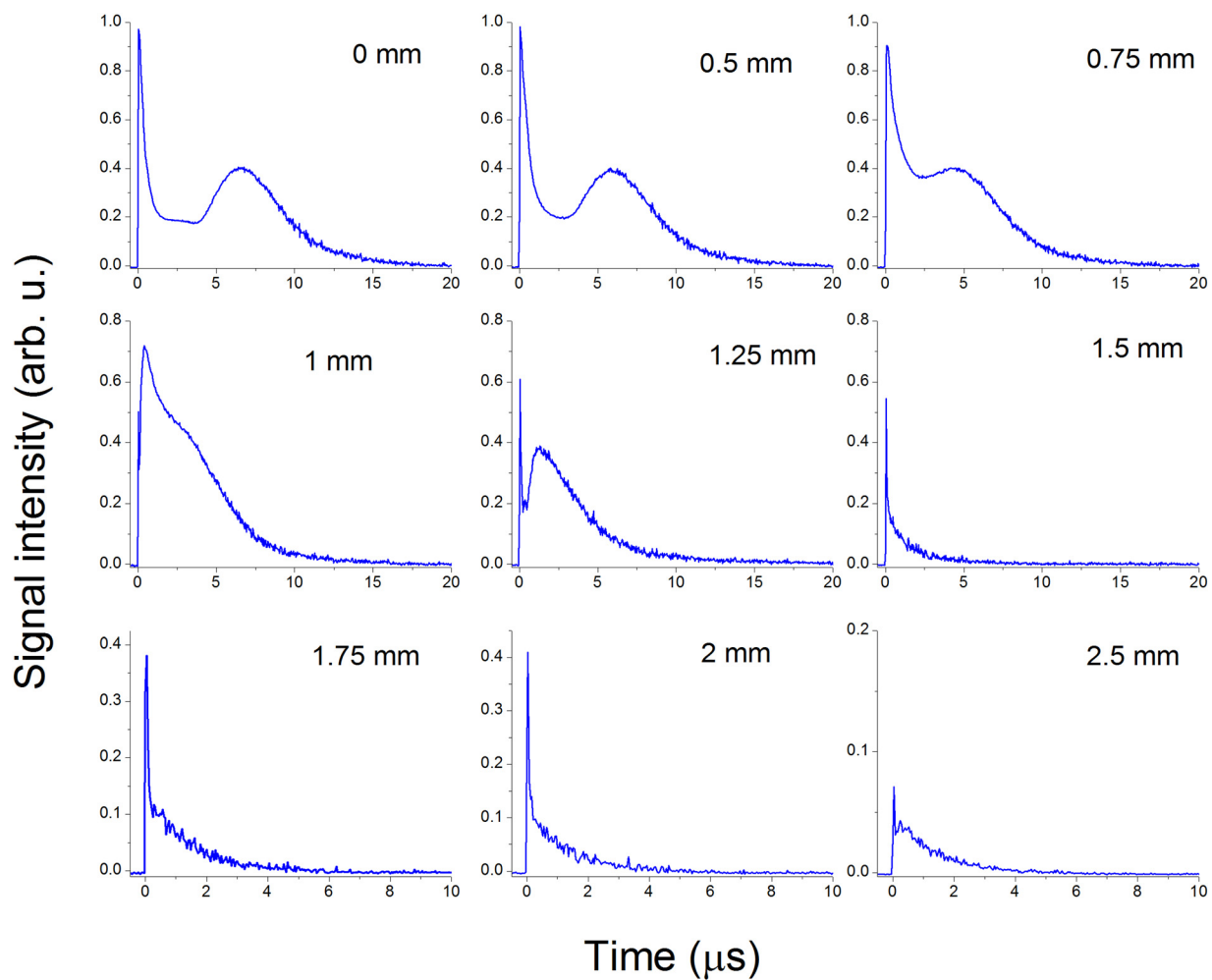


FIG. 12. Temporal emission features of O I at 777.2 nm at various spatial points from the plasma kernel central position.

eventually disappears at larger distances. For example, the O I emission reaches a maximum at $\sim 4 \mu\text{s}$ and $\sim 1.75 \mu\text{s}$ for 0.75 mm and 1.25 mm distances, respectively. The reduction in the peak time with increasing distance can be correlated to a rapid decrease in temperature with increasing separation from the kernel center plane, which in effect reduces the persistence of O species. A triple peak temporal history can be seen at distances ~ 1 mm. At these distances, a sharp prompt peak followed by another intermediate peak is observed before the broad temporal delayed peak. The observed arrival time of the new peak is observed at 1 mm ~ 340 ns, which is consistent with arrival time of shock waves using shadowgraphy. Considering the estimated shock temperature (Fig. 5) is significantly lower compared to dissociation energy of O₂ molecules⁵¹ (5.15 eV), it is conjectured that the shock heating alone may not be the reason for intense O I lines seen at farther distances from the plasma kernel. However, the shock wave heating occurs after UV excitation produced by the spark, and hence a synergistic effect of UV radiation and shock heating on ambient dissociation and excitation is not ruled out and further studies in this context are necessary.

IV. SUMMARY

We investigated the lifecycle of air sparks produced by ns lasers using various plasma diagnostic tools. The studies

provide information of the air spark's early time dynamics, decoupling of the shock wave from the plasma core, emission from the spark kernel, cold gas excitation by UV radiation, gas heating by shock waves, and onset of turbulence in the plasma region. The focused shadowgraphy employing varying magnifications enabled visualization of the transient nature of spark generation, internal structures, asymmetric expansion, and turbulence. The temperature and pressure of the shock layer decreases rapidly after the termination of the laser pulse. Consequently, the shock expansion velocity is also decreased in all directions. The shadowgraphic and self-emission images showed that the spark possesses a cylindrical shape at early times ($\leq 1 \mu\text{s}$). The asymmetric morphology of the spark at early times is caused by preferential absorption of the incoming laser beam by the spark front facing the beam. The spark showed different morphologies in the midlife ($\sim 10 \mu\text{s}$) for shock propagation (spherical shape) and for self-emission (triangular shape). At the end of the lifecycle, the air spark showed turbulent structures. Both imaging techniques showed that the sparks expanded with a supersonic velocity at early times ($\leq 1 \mu\text{s}$) and transitioned to sonic velocities at later times. The shadowgram images also showed that the shock waves decouple from the hot core plasma at times $\geq 1 \mu\text{s}$. During this time frame, the self-emission images showed suppression of the spark expansion and obtained a triangular shape.

Time and space resolved emission analysis were used for differentiating various excitation mechanisms in the air spark. The spectral details showed continuum emission at earliest times followed by ionic, atomic, and molecular emission from the spark kernel. The later time ($\geq 10 \mu\text{s}$) spectroscopic analysis of the plasma kernel showed intense emission from N_2^+ (B-X) and CN (B-X) molecular bands along with isolated O I and N I lines. The atomic and molecular spectral features observed at time $\sim 10 \mu\text{s}$ were simulated using SPECAIR and showed excellent agreement using a temperature $\sim 7000 \text{ K}$. The spectral data also provided details about UV excitation of cold air produced by the spark at earlier times. The spectral details measured at various spatial locations and times away from the kernel showed very complex features, which include broadband-like emission mixed with absorption dips, superimposed with atomic and molecular emission lines and bands. Further radiation transport modeling studies at atmospheric conditions are necessary to explain some of the observed spectral features and will be the focus of future work.

The space resolved O I persistence data showed multiple temporal distributions. The temporal history of the O I line at the kernel mid plane (0 mm) showed an intense sharp peak following by a broad temporal emission peak, which persisted beyond $20 \mu\text{s}$. The sharp peak, which appeared at all distances immediately after laser firing, could be due to broadband emission caused by bremsstrahlung by the plasma kernel at short distances and by UV excitation at larger distances, and the delayed peak is caused by the excitation of O I atoms by the plasma kernel. A triple fold temporal history seen at distances $\sim 1 \text{ mm}$ with the occurrence of an intermediate peak between the bremsstrahlung and kernel excitation peak assigned to shock heating and subsequent excitation.

The present results clearly demonstrate the importance of using multiple diagnostic tools with high temporal and spatial resolution for probing highly transient and complex plasma systems. The emission spectroscopic studies combined with fast gated self-emission images and focused shadowgraphy provided significant insights regarding the various physical and chemical processes happening in the spark kernel and surrounding medium. It also highlights the complexity of separating various excitation mechanisms in a laser generated air spark. In particular, studies probing the temporal and spatial dependence of the formation mechanisms for various transient species, which strongly depends on local plasma parameters, are crucial. Hence, future experiments will be focused on characterizing the plasma parameters at various spatial locations at and away from the spark kernel to identify spatial and temporal correlations to emission from excited molecular and atomic species.

ACKNOWLEDGMENTS

This work was supported by the DOE/NNSA Office of Nonproliferation and Verification Research and Development (NA-22). The Pacific Northwest National Laboratory was operated for the U.S. Department of Energy (DOE) by the Battelle Memorial Institute under Contract No. DE-AC05-

76RL01830. We thank Bret D. Cannon for valuable discussions, while preparing the manuscript.

- ¹L. Radziemski and D. Cremers, "A brief history of laser-induced breakdown spectroscopy: From the concept of atoms to LIBS 2012," *Spectrochim. Acta, Part B* **87**, 3 (2013).
- ²J. P. Singh and S. N. Thakur, *Laser Induced Breakdown Spectroscopy* (Elsevier, Amsterdam, 2007).
- ³S. Musazzi and U. Perini, *Laser-Induced Breakdown Spectroscopy—Fundamentals and Applications* (Springer Series in Optical Sciences, 2014).
- ⁴D. W. Hahn and N. Omenetto, "Laser-induced breakdown spectroscopy (LIBS), Part II: Review of instrumental and methodological approaches to material analysis and applications to different fields," *Appl. Spectrosc.* **66**(4), 347 (2012).
- ⁵U. Verma and A. K. Sharma, "Laser frequency upshift and self-defocusing under avalanche breakdown of air," *Phys. Plasmas* **17**(12), 123101 (2010).
- ⁶R. C. Issac, P. Gopinath, G. K. Varier, V. P. N. Nampoori, and C. P. G. Vallabhan, "Twin peak distribution of electron emission profile and impact ionization of ambient molecules during laser ablation of silver target," *Appl. Phys. Lett.* **73**(2), 163 (1998).
- ⁷S. Ratynskaia, G. Dilecce, and P. Tolias, "Nitrogen optical emission during nanosecond laser ablation of metals: Prompt electrons or photo-ionization?", *Appl. Phys. A* **117**(1), 409 (2014).
- ⁸N. Glumac, G. Elliott, and M. Boguszko, "Temporal and spatial evolution of a laser spark in air," *AIAA Journal* **41**(9), 1984–1994 (2005).
- ⁹S. S. Harilal, G. V. Miloshevsky, P. K. Diwakar, N. L. LaHaye, and A. Hassanein, "Experimental and computational study of complex shockwave dynamics in laser ablation plumes in argon atmosphere," *Physics of Plasmas* **19**(8) 083504 (2012).
- ¹⁰S. Amoruso, M. Armenante, R. Buzzese, N. Spinelli, R. Velotta, and X. Wang, "Emission of prompt electrons during excimer laser ablation of aluminum targets," *Appl. Phys. Lett.* **75**(1), 7 (1999).
- ¹¹A. P. Yalin, N. Wilvert, C. Dumitache, S. Joshi, and M. N. Shneider, "Laser plasma formation assisted by ultraviolet pre-ionization," *Phys. Plasmas* **21**(10), 103511 (2014).
- ¹²K. E. Harwell and R. G. Jahn, "Initial ionization rates in shock heated Ar, Kr, and Xe," *Phys. Fluids* **7**(2), 214 (1964).
- ¹³Y. P. Raizer, "Heating of a gas by a powerful laser pulse," Sov. Phys. JETP **21**(5), 1009 (1965).
- ¹⁴C. G. Parigger, G. M. Guan, and J. O. Hornkohl, "Measurement and analysis of OH emission spectra following laser-induced optical breakdown in air," *Appl. Opt.* **42**(30), 5986 (2003).
- ¹⁵J. J. Camacho, L. Diaz, M. Santos, L. J. Juan, and J. M. L. Poyato, "Time-resolved optical emission spectroscopy of laser-produced air plasma," *J. Appl. Phys.* **107**(8), 083306 (2010).
- ¹⁶M. Thiagarajan and J. Scherer, "Experimental investigation of ultraviolet laser induced plasma density and temperature evolution in air," *J. Appl. Phys.* **104**(1), 013303 (2008).
- ¹⁷R. Tambay and R. K. Thareja, "Laser-induced breakdown studies of laboratory air at 0.266, 0.355, 0.532, and 1.06 μm ," *J. Appl. Phys.* **70**(5), 2890 (1991).
- ¹⁸T. X. Phuoc, "Laser-induced spark ignition fundamental and applications," *Opt. Laser Eng.* **44**(5), 351 (2006).
- ¹⁹R. Tambay, D. V. S. Muthu, V. Kumar, and R. K. Thareja, "Laser-induced air breakdown using 0.355, 0.532, and 1.06 μm radiation," *Pramana-J. Phys.* **37**(2), 163 (1991).
- ²⁰J. B. Simeonsson and A. W. Mizolek, "Spectroscopic studies of laser-produced plasmas formed in Co and Co₂ using 193, 266, 355, 532, and 1064 nm laser-radiation," *Appl. Phys. B* **59**(1), 1 (1994).
- ²¹C. V. Bindhu, S. S. Harilal, M. S. Tillack, F. Najmabadi, and A. C. Gaeris, "Energy absorption and propagation in laser-created sparks," *Appl. Spectrosc.* **58**(6), 719 (2004).
- ²²V. Hohreiter, A. J. Ball, and D. W. Hahn, "Effects of aerosols and laser cavity seeding on spectral and temporal stability of laser-induced plasmas: Applications to LIBS," *J. Anal. At. Spectrom.* **19**(10), 1289 (2004).
- ²³Y. L. Chen, J. W. L. Lewis, and C. Parigger, "Spatial and temporal profiles of pulsed laser-induced air plasma emissions," *J. Quant. Spectrosc. Radiat. Transfer* **67**(2), 91 (2000).
- ²⁴Y. P. Raizer, *Gas Discharge Physics* (Springer-Verlag, Berlin, Germany, 1991).
- ²⁵M. Thiagarajan and J. E. Scherer, "Experimental investigation of 193-nm laser breakdown in air," *IEEE Trans. Plasma Sci.* **36**(5), 2512 (2008).

- ²⁶H. Zhang, J. Lu, and X. Ni, "Optical interferometric analysis of colliding laser produced air plasmas," *J. Appl. Phys.* **106**(6), 063308 (2009).
- ²⁷S. Yalcin, D. R. Crosley, G. P. Smith, and G. W. Faris, "Influence of ambient conditions on the laser air spark," *Appl. Phys. B* **68**(1), 121 (1999).
- ²⁸V. I. Bergel'son, T. V. Loseva, I. V. Nemchinov, and T. I. Orlova, "Propagation of plane supersonic radiation waves," Sov. J. Plasma Phys. **1**, 498 (1975).
- ²⁹W. Fox, G. Fiksel, A. Bhattacharjee, P. Y. Chang, K. Germaschewski, S. X. Hu, and P. M. Nilson, "Filamentation instability of counterstreaming laser-driven plasmas," *Phys. Rev. Lett.* **111**(22), 225002 (2013).
- ³⁰A. N. Mostovych, B. H. Ripin, and J. A. Stamper, "Laser-produced plasma jets—Collimation and instability in strong transverse magnetic-fields," *Phys. Rev. Lett.* **62**(24), 2837 (1989).
- ³¹J. R. Wilson, "Laser-induced gas breakdown," *J. Phys. D* **3**, 2005 (1970).
- ³²P. Gregorcic, J. Diaci, and J. Mozina, "Two-dimensional measurements of laser-induced breakdown in air by high-speed two-frame shadowgraphy," *Appl. Phys. A* **112**(1), 49 (2013).
- ³³K. Takahashi, K. Maeda, T. Ikuta, S. Hatano, Y. Mori, and K. Nagayama, "Transient structure of ionized atmosphere in pulsed laser propulsion system," *Proc. SPIE* **4183**, 907 (2001).
- ³⁴H. U. Rahman, P. Ney, N. Rostoker, A. Van Drie, and F. J. Wessel, "Control of the Rayleigh-Taylor instability in a staged Z pinch," *Phys. Plasmas* **11**(12), 5595 (2004).
- ³⁵H. Sobral, M. Villagran-Muniz, R. Navarro-Gonzalez, and A. C. Raga, "Temporal evolution of the shock wave and hot core air in laser induced plasma," *Appl. Phys. Lett.* **77**(20), 3158 (2000).
- ³⁶M. Villagran-Muniz, H. Sobral, and E. Camps, "Shadowgraphy and interferometry using a CW laser and a CCD of a laser-induced plasma in atmospheric air," *IEEE Trans. Plasma Sci.* **29**(4), 613 (2001).
- ³⁷I. G. Dors and C. G. Parigger, "Computational fluid-dynamic model of laser-induced breakdown in air," *Appl. Opt.* **42**(30), 5978 (2003).
- ³⁸R. Joarder, G. C. Gebel, and T. Mosbach, "Two-dimensional numerical simulation of a decaying laser spark in air with radiation loss," *Int. J. Heat Mass Transfer* **63**, 284 (2013).
- ³⁹Y. B. Zeldovich and Y. P. Raizer, *Physics of Shock Waves and High-Temperature Hydrodynamic Phenomena* (Dover, New York, 2002).
- ⁴⁰G. Taylor, "The formation of a blast wave by a very intense explosion. 1. Theoretical discussion," *Proc. R. Soc. London, Ser. A* **201**(1065), 159 (1950).
- ⁴¹A. Chen, Y. Jiang, H. Liu, M. Jin, and D. Ding, "Plume splitting and rebounding in a high-intensity CO₂ laser induced air plasma," *Phys. Plasmas* **19**(7), 073302 (2012).
- ⁴²C. Li, J. M. Wang, and X. W. Wang, "Shock wave confinement-induced plume temperature increase in laser-induced breakdown spectroscopy," *Phys. Lett. A* **378**(45), 3319 (2014).
- ⁴³J. A. Aguilera and C. Aragon, "Characterization of laser-induced plasma during its expansion in air by optical emission spectroscopy: Observation of strong explosion self-similar behavior," *Spectrochim. Acta, Part B* **97**, 86 (2014).
- ⁴⁴L. J. Radziemski, T. R. Loree, D. A. Cremers, and N. M. Hoffman, "Time-resolved laser-induced breakdown spectrometry of aerosols," *Anal. Chem.* **55**(8), 1246 (1983).
- ⁴⁵C. O. Laux, T. G. Spence, C. H. Kruger, and R. N. Zare, "Optical diagnostics of atmospheric pressure air plasmas," *Plasma Sources Sci. Technol.* **12**(2), 125 (2003).
- ⁴⁶SPECAR Version 3.0.2.0, Spectralfit S.A.S, 2012.
- ⁴⁷N. Farid, S. S. Harilal, H. Ding, and A. Hassanein, "Kinetics of ion and prompt electron emission from laser-produced plasma," *Phys. Plasmas* **20**, 073114 (2013).
- ⁴⁸V. Bakshi, *EUV Lithography* (SPIE, WA, 2008).
- ⁴⁹S. S. Harilal, G. V. Miloshevsky, T. Sizuk, and A. Hassanein, "Effects of laser wavelength on water-window Ly-alpha and He-alpha line emission from nitrogen plasma," *Phys. Plasmas* **20**(1), 013105 (2013).
- ⁵⁰H. Cronberg, M. Reichling, E. Broberg, H. B. Nielsen, E. Matthias, and N. Tolk, "Effects of inverse bremsstrahlung in laser-induced plasmas from a graphite surface," *Appl. Phys. B* **52**(3), 155 (1991).
- ⁵¹S. J. Blanksby and G. B. Ellison, "Bond dissociation energies of organic molecules," *Acc. Chem. Res.* **36**(4), 255 (2003).